A&A 471, 561–571 (2007)
DOI: 10.1051/0004-6361:20067034

Astronomy & Astrophysics

CO and CS in the Magellanic Clouds: a χ^2-analysis of multitransitional data based on the MEP radiative transfer model*

S. Nikolić[1], G. Garay[1], M. Rubio[1], and L. E. B. Johansson[2]

[1] Departamento de Astronomía, Universidad de Chile, Casilla 36-D, Santiago, Chile
e-mail: `silvana@das.uchile.cl`
[2] Onsala Space Observatory, S-43992 Onsala, Sweden

Received 27 December 2006 / Accepted 30 April 2007

ABSTRACT

Aims. Our goal is to determine the physical properties of molecular gas located in different environments of the SMC – from near the vicinity of hot H II regions to cold, quiescent clouds – via modelling and simulations, and compare with the properties of molecular gas found in similar environments in the LMC.
Methods. We present observations of the ^{12}CO (1–0), (2–1), (3–2), ^{13}CO (1–0), (2–1), and CS (2–1), (3–2) line emission toward six molecular clouds in the SMC: N 66, N 88, Lirs 36, Lirs 49, Hodge 15, and SMC-B1#1. These data, as well as published data on three clouds of the LMC: 30 Dor-10, N 159-W, and N 159-S, are analysed to estimate gas kinetic temperatures, column densities, and surface filling factors using a Mean Escape Probability approximation of the radiative transfer equations. The solutions are restricted using the χ^2 approach.
Results. Assuming that the [^{12}CO/^{13}CO] abundance ratio is similar in both galaxies, we find that the CO and CS column densities of SMC clouds are a magnitude smaller than those of LMC clouds, mirroring the metallicity differences. Our analysis suggests the existence of a lower limit for the ^{12}CO/^{13}CO isotope ratio of 50 in both galaxies. The surface filling factors of the CO emission in the SMC clouds are a factor of a few smaller than in the LMC and seem to decrease with increasing UV radiation fields, i.e., more vigorous star formation activity.
A simple model, which assumes a spherical cloud with uniform physical parameters immersed in the CMB radiation field, provides a reasonably good fit to the observed properties of the (supposedly) quiescent clouds SMC-B1#1 and N 159-S. For all other clouds considered, this model gives large values of χ^2, strongly indicating the need for a more complex model. We present some results from 2-component modelling, e.g., for Lirs 36 a mixture of 20 K gas with high optical depth and a less dense gas with temperatures of 100 K reproduces well the main features of the CO data.

Key words. ISM: clouds – ISM: molecules – galaxies: ISM – galaxies: Magellanic Clouds

1. Introduction

The proximity of the Magellanic Clouds gives us an excellent opportunity to study in detail galaxies that are considerably different from our own. Numerous studies of stars and clusters have long ago established that both, the Large and the Small Magellanic Clouds are extremely metal- and dust-deficient (e.g. Westerlund 1990). Regarding the star formation history in the SMC, recent studies have found evidence for two "star-burst" events, ~6.5 and 2.5 Gyr ago (Piatti et al. 2005) – the latter probably has an origin in a very close encounter of the LMC and the SMC, of which the so-called Wing is a remnant. Vigorous ongoing star formation produces high, as compared to the Solar Neighbourhood, (UV) radiation densities.

Only with the advent of the SEST telescope the spatial resolution necessary for studies of these stellar nurseries, namely individual molecular clouds was achieved. A wealth of data collected over several years under the ESO-Swedish/SEST Key Programme "CO in the Magellanic Clouds" was presented and discussed in a sequence of papers starting from the first CO survey of the LMC and SMC (Israel et al. 1993). The first fully sampled ^{12}CO (1–0) and (2–1) maps of six molecular clouds in the SMC were presented in Rubio et al. (1996). Physical properties of those clouds were discussed in Lequeux et al. (1994). Johansson et al. (1998) observed and analyzed CO data up to $J = 3 \rightarrow 2$ of the 30 Dor region in the LMC. Extended ^{12}CO (1–0) and (2–1) maps of several star-forming regions were given in Israel et al. (2003). Both the LMC and the SMC were also observed in several other molecules and a variety of transitions, e.g., Heikkilä et al. (1999). Although the Key Programme itself was concluded in 1995, the SEST observations of the Magellanic Cloud have continued, part of which we present here.

1.1. Sample clouds

Table 1 summarizes some of the basic parameters of the SMC molecular clouds investigated here. Column 1 gives the cloud name used here as well as other known designations, mainly those of associated H II regions. The center coordinates are, however, not necessarily coincident. Labels "N" and "DEM" refer to sources found in surveys of H_α-emission stars and nebulae towards the Magellanic Clouds by Henize (1956) and Davies et al. (1976), respectively. The FIR sources of

---

* The observations were made with the Swedish-ESO Submillimetre Telescope, SEST, which was operated jointly by the Swedish National Facility for Radioastronomy and the ESO.

Table 1. The peak coordinates of the molecular clouds observed and their estimated sizes: a) from Lequeux et al. (1994) and b) from Israel et al. (2003).

Cloud	α (1950.0)	δ (1950.0)	R [pc]
N 66/DEM 103	00:57:39.7	–72:25:16	12^a
N 88/DEM 161/Lirs 215	01:22:54.0	–73:24:33	5^b
Lirs 36/N 12/DEM 23	00:44:51.7	–73:22:28	7^b
Lirs 49/N 27/DEM 40	00:46:32.9	–73:21:50	10^b
Hodge 15	00:46:23.0	–73:39:10	18^a
SMC-B1#1	00:43:42.0	–73:35:10	10^a

Schwering & Israel (1989) are denoted with "Lirs". Columns 2 and 3 give the coordinates of the peak CO emission (Rubio et al. 1996).

The *N66* complex in the "Bar" is by far the most luminous H II region in the SMC (Caplan et al. 1996). The molecular cloud in our sample is located towards the NE of the H II complex. Rubio et al. (2000) mapped the ^{12}CO(2–1) line emission across the whole region. Their channel maps suggest that there is no physical connection between the molecular gas in our cloud N 66 NE and the H II complex itself.

N88 in the "Wing" seems to be the hottest and the most reddened H II region in the SMC (e.g., Wilcots 1994; Caplan et al. 1996). The H II region is centered on the SW edge of the associated CO cloud, the molecular cloud actually being smaller.

Lirs 36 is a moderately bright complex (Caplan et al. 1996) that contains two distinct H II regions, *A* and *B*. The former is centered at the western edge of the associated CO molecular cloud (Rubio et al. 1996; Israel et al. 2003). Chin et al. (1998) have observed this cloud in a number of different molecular lines.

Lirs 49 is, according to the detected H_α flux, among the most obscured H II regions in the SMC (Caplan et al. 1996). The associated molecular cloud, west of the nebula, is the brightest CO cloud in the SMC (Rubio et al. 1996). The region was studied in detail in several molecular transitions by Heikkilä et al. (1999).

Hodge 15, first detected as a $3' \times 1'$ low opacity dark nebulosity by Hodge (1974), is thought to be a quiescent cloud without any signs of star formation. Schwering & Israel (1989) however detected a FIR source at about $1'$ off the peak opacity coordinates. Wilke et al. (2003) re-examined the HiRes 60 – and 100 μm IRAS maps of the region and found a cold FIR source, with an estimated dust temperature of $T_\mathrm{d} \approx 30$ K, just $30''$ off the CO peak.

SMC-B1#1 is an isolated CO cloud north of the SMC-B1 molecular cloud complex (Rubio et al. 1993, 1996, 2004). The cloud is coincident with a second entry in Hodge (1974), a $2' \times 1'$ very opaque dark nebulae.

Column 4 of Table 1 gives the estimated cloud sizes (Lequeux et al. 1994; Israel et al. 2003). In the former reference radii are defined via an integrated line-flux threshold (3σ) of the ^{12}CO (1–0) line emission of 0.4 K km s^{-1} (Rubio et al. 1993). The latter authors determined the cloud radii by counting the pixels with significant ^{12}CO (1–0) emission (N) and taking $r = (N/\pi)^{0.5}\,\Delta S$, where ΔS is the linear grid spacing, usually $20''$. The results were then corrected for finite beamwidth. Fully sampled ^{12}CO (1–0) and (2–1) line profile maps of all six clouds are presented in Rubio et al. (1996). Their physical properties based on the then available ^{12}CO and ^{13}CO line ratios are discussed in Lequeux et al. (1994). CO maps and position velocity diagrams of Lirs 36, Lirs 49 and N 88 were presented in Israel et al. (2003).

In this paper we present new observations of the emission in the ^{12}CO (3–2) and the CS (2–1) and (3–2) transitions from these six molecular clouds. We then analyze the data on all the available transitions of ^{12}CO, ^{13}CO, and CS towards these clouds using the Mean Escape Probability approximation of the radiative transfer equations. The final solutions are obtained using the χ^2 approach. We also reanalyse previously published data of LMC molecular clouds using the same approach, in order to assess possible differences between the two galaxies. As for the SMC cloud sample, the LMC clouds considered here cover a wide range of environments, from the most spectacular star-forming region in the Local Group, the 30 Doradus nebula, to a quiescent cloud in the N 159 area. In order of star formation activity, the clouds are 30 Dor-10, N 159-W, and N 159-S (Johansson et al. 1998).

2. Observations

All six clouds of the sample presented here were previously observed at SEST in the CO (1–0), CO (2–1), ^{13}CO (1–0), and ^{13}CO (2–1) lines (Rubio et al. 1996). The new data incorporated in this study include observations of the CO (3–2) line at 350 GHz, using the NDW350 receiver, and CS (2–1) and CS (3–2) lines using the SESIS100 (or IRAM115) and SESIS150 receivers, respectively. Observations were done in beam-switching mode. The two CS transitions were observed simultaneously in all but one source, Hodge 15. Typical system temperatures were 1000, 180 and 150 K at 345, 147 and 98 GHz, respectively. The main beam efficiencies adopted are 0.74, 0.66, 0.60 and 0.33 at 100, 147, 230 and 345 GHz; the corresponding HPBWs are $50''$, $34''$, $23''$, and $15''$. To reach an rms sensitivity of about 10 mK in CO, we spent between 50 and 460 min on-source. The reduction was done using CLASS packages and standard procedures. The CO (3–2) emission was mapped within a region of $30'' \times 30''$ with $10''$ spacing centered on the CO (1–0) peak, allowing a proper estimate of the CO (1–0) beam response. No mapping was done in the CS lines. To "mimic" the response of the CS (2–1) beam, the intensities of the CS (3–2) lines were scaled by 0.7, a factor consistent with those applied by Heikkilä et al. (1999). For a sample of clouds in the LMC they found factors in the range 0.55 to 0.80, and a factor 0.7 for Lirs 49 in the SMC. Final spectra, convolved to the same resolution, are shown in Fig. 1.

3. Modelling

3.1. The MEP model

A non-LTE excitation and radiative transfer code, RADEX (Jansen et al. 1994), was employed to analyze the CO and CS emissions. The model uses the mean escape probability approximation (MEP) for the radiative transfer equations, which effectively decouples the radiation from molecular excitation. This enables us to include background radiation. The program includes collisions, spontaneous and stimulated radiative transitions and computes statistical equilibrium for rotational levels of interstellar molecules and predicts line brightness temperatures. Clouds are assumed to be spherical, homogeneous, isothermal, with constant density and abundances. The escape probability used is that of uniform sphere (Osterbrock 1974). The optical depth in the line center, and consequently the escape probability

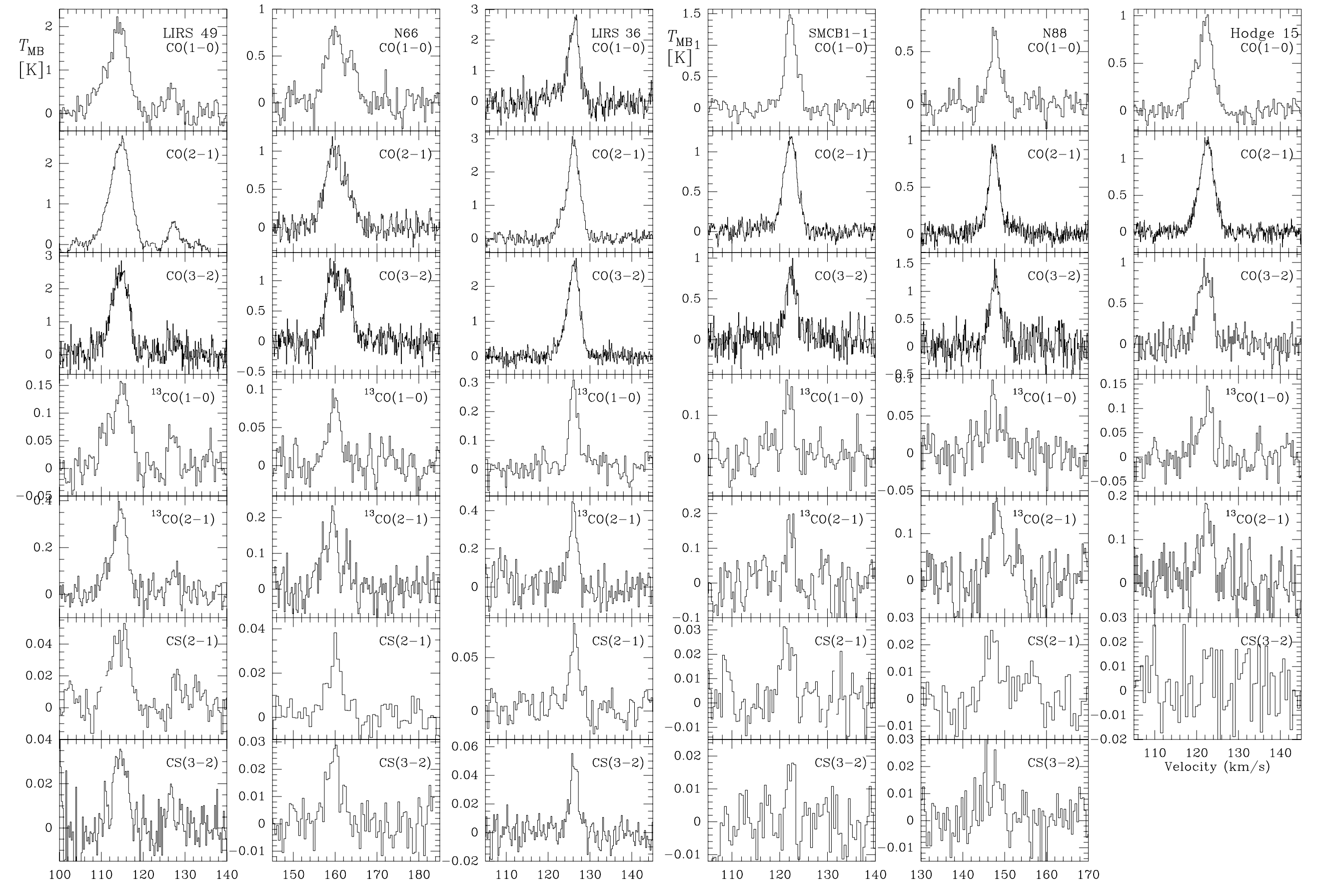

Fig. 1. The observed spectra of the clouds in the main beam brightness temperature scale. The higher transitions CO spectra are convolved to the CO(1–0) beam size of 45″ and the CS (3–2) spectra are scaled by 0.7 to "mimic" the beam response of the CS (2–1) line.

depends only on the $N/\Delta v$ ratio, where N is the total column density of the molecule and Δv the FWHM of the line.

As background radiation field we considered only the microwave background (T_{CBG} = 2.73 K). Thus the internal radiation field used to find solutions of the statistical equilibrium equations for the level populations is

$$I_\nu = \beta \left[B_\nu(T_{\mathrm{CBG}}) \right] + (1 - \beta)\, B_\nu(T_{\mathrm{ex}}), \tag{1}$$

where β is the escape probability. We note that for some sources, depending on the characteristics of their environment, additional contribution to the background emission (e.g., dust and free-free emission) might be significant.

3.2. The modelled parameter space

For the CO isotopes we considered kinetic temperatures in the range from 5 to 500 K (with the step of $\log\,[T_{\mathrm{kin}}] = 0.05$), column densities from 10^{14} to 5×10^{22} cm^{-2} for ^{12}CO and from 10^{12} to 10^{21} cm^{-2} for ^{13}CO with a grid spacing of $\log\,[N(\mathrm{CO})] = 0.1$ in both cases. For the hydrogen molecule number density – the main and only collisional partner considered – we investigated the range $n(\mathrm{H_2}) = 10^3$–10^7 cm^{-3} with a step of $\log\,[n(\mathrm{H_2})] = 0.5$. The CS parameter space considered was T_{kin} = 5–25 K, $n(\mathrm{H_2}) = 3 \times 10^3$–$10^8$ cm^{-3} and $N(\mathrm{CS}) = 10^{11}$–10^{16} cm^{-2} with the same steps in the variables as above. The statistical equilibrium calculation included 325 transitions among 26 levels and 78 transitions among 13 levels, for CO and CS respectively.

We adopted the collisional rate coefficients calculated by Flower (2001) for CO and Turner (1992) for CS. This set of collision coefficients is also used in the on-line version of the RADEX code. Schöier et al. (2005) briefly discussed the accuracy of adopted rate coefficients. For collisions with para-H$_2$ compared with ortho-H$_2$ at the low temperatures typical of dark clouds, line intensities of the higher transitions can differ up to ±150%. In the original RADEX code of Jansen et al. (1994) the collisional rate coefficients for CO were those of Schinke et al. (1985) and for CS those of Green & Chapman (1978). We have compared the line intensities computed using the different sets of collisional rate coefficients for a range of kinetic temperatures, column densities, and hydrogen number densities typical for dark clouds. In the case of CO up to the $J = 5 \rightarrow 4$ transition, the line intensities agree within 25–30% and the difference grows larger for higher transitions. For a fixed kinetic temperature and a fixed CO column density, the difference increases as the density decreases. However, when considering ratios of line intensities from transitions with low J numbers, each set of collisional rate coefficients gives essentially the same result. Comparison shows that the difference of line intensity ratios for the first four transitions is ∼10%. The CS (3–2)/CS (2–1) intensity ratios, which are used in this paper, show in some cases larger differences than the CO depending on the adopted collisional rates. The difference is about 30% for T_{kin} = 5 K and $n(\mathrm{H_2}) = 10^4$ cm^{-3} but decreases with increasing temperatures and densities. For example, the difference is less than 5% for T_{kin} = 20 K and $n(\mathrm{H_2}) \geq 10^5$ cm^{-3} for a wide range of CS column densities.

Table 2. The CO and CS observed line integrated intensities in $T_{\rm mb}\,\Delta v$ [K km s^{-1}] and the CO (1–0) linewidth in [km s^{-1}]. Errors quoted in the brackets are noise contribution determined by Gaussian fits. All intensities refer to the CO (1–0) or CS (2–1) beam sizes.

	CO			^{13}CO		CS		
Cloud	$J = 1 \to 0$	$J = 2 \to 1$	$J = 3 \to 2$	$J = 1 \to 0$	$J = 2 \to 1$	$J = 2 \to 1$	$J = 3 \to 2$	Δv
N 66 c1[a]	1.1 (0.2)	1.1 (0.3)	2.3 (0.2)	0.02 (0.01)	0.13 (0.04)	<0.01	<0.01	2.4(0.4)
c2	3.6 (0.3)	4.8 (0.4)	4.4 (0.3)	0.28 (0.03)	0.73 (0.07)	0.11 (0.01)	0.09 (0.01)	4.6(0.4)
N 88	1.93 (0.09)	2.61 (0.05)	3.7 (0.2)	0.29 (0.02)	0.44 (0.06)	0.09 (0.01)	0.05 (0.01)	3.0(0.2)
Lirs 36	8.8 (0.3)	10.5 (0.1)	9.1 (0.1)	0.74 (0.04)	1.10 (0.08)	0.18 (0.01)	0.10 (0.01)	3.4(0.2)
Lirs 49 c1[b]	11.3 (0.3)	13.9 (0.1)	12.2 (0.3)	0.76 (0.05)	1.44 (0.07)	0.25 (0.01)	0.12 (0.01)	6.2(0.3)
c2	1.4 (0.2)	1.34 (0.05)	1.3 (0.2)	0.20 (0.03)	0.21 (0.04)	0.08 (0.01)	0.03 (0.01)	5.9(0.3)
Hodge 15	4.4 (0.1)	4.81 (0.05)	3.4 (0.2)	0.52 (0.05)	0.56 (0.07)	–	0.04 (0.02)	4.6(0.2)
SMC-B1#1	4.0 (0.1)	3.10 (0.08)	2.2 (0.1)	0.37 (0.04)	0.29 (0.06)	0.08 (0.01)	0.04 (0.02)	2.7(0.2)

[a] N 66 c1: $v_{\rm LSR} = 163.2$ km s^{-1}, c2: $v_{\rm LSR} = 159.4$ km s^{-1}. [b] Lirs 49 c1: $v_{\rm LSR} = 114.3$ km s^{-1}, c2: $v_{\rm LSR} = 127.4$ km s^{-1}.

3.3. χ^2 analysis

Since the surface filling factor of the molecular line emission is unknown, a common method is to use intensity ratios to determine physical parameters of the interstellar gas. Such a procedure, also using RADEX, was previously applied to molecular line data in the Magellanic Clouds by, e.g., Johansson et al. (1998), Heikkilä et al. (1999), and Bolatto et al. (2005). In this paper we restrict the range of solutions by using the χ^2 approach. However, lacking ^{13}CO(3–2) data, ratios do not (easily) allow equal weights of the transitions observed. A more straightforward way, used here, to define χ^2 is:

$$\chi^2 = \sum_n \left[\frac{sff \times I^{(n)}_{\rm mod} - I^{(n)}_{\rm obs}}{\Delta I^{(n)}_{\rm obs}} \right]^2 \tag{2}$$

where $I^{(n)}_{\rm mod}$ and $I^{(n)}_{\rm obs}$ are the model and observed intensities (see Table 2), respectively, $\Delta I^{(n)}_{\rm obs}$ is the corresponding 1σ error estimate of the observations, and *sff* is the surface filling factor of the emission assumed to be equal for all transitions; *sff* is varied to minimize χ^2. One restriction for a solution is obviously that $sff \leq 100\%$. The column density of CO is then calculated as

$$N({\rm CO}) = \left[N({\rm CO})/\Delta v\right]_{\rm mod} \times \Delta v_{\rm obs} \times sff, \tag{3}$$

where $\Delta v_{\rm obs}$ is the observed linewidth.

The CO intensity errors have a contribution from both a random part ($\sigma_{\rm rms}$, determined from the Gaussian fits; see Table 2) and a systematic part due mainly to uncertainties in the beam efficiency ($\sigma_{\rm beff}$), which includes intensity calibration errors. For transitions higher than $J = 1 \to 0$, the errors are dominated by the latter component. For the beam uncertainties we use the estimates of Johansson et al. (1998) of 20% and 30% for the $J = 2 \to 1$ and $J = 3 \to 2$ transitions, respectively, and consider those as 3σ levels. The total error is then estimated as $\Delta I_{\rm obs} = (\sigma^2_{\rm rms} + \sigma^2_{\rm beff})^{1/2}$. Formally, χ^2 values of 5 and 10 correspond to confidence levels of about 95% and 60%, respectively. Thus, provided that the errors are reasonably well estimated, solutions with $\chi^2 \geq 10$ strongly suggest that the applied model is not an appropriate one. At least three clouds in our sample appear to be far more complex than the model assumes: N 88 and Lirs 49 c1 in the SMC and 30 Dor–10 in the LMC. To classify the sources with respect to model assumptions we used as an additional criteria isotopic ratio constraints (see the following section). When it seems that a cloud is reasonably well described by the model, we quote errors determined by $\chi^2 = 5$. For the remaining sources we restrict, somewhat arbitrarily, the range of solutions by the condition $\chi^2 \leq 2\chi^2_{\rm min}$. This provides information about the relative accuracy between the parameters derived. The errors in CO column densities are, typically, a factor of three smaller than those of kinetic temperatures and surface filling factors.

The total CS intensity errors are dominated by the random part. We ran the RADEX code for CS which produces the same output as in the CO case. However, since just two transitions are involved, we present only column density results; kinetic temperatures and filling factors are strongly dependent on the molecular hydrogen density. We used $n({\rm H_2})$ between 10^4 and 10^7 cm^{-3}. The derived CS column density ranges are defined by the 2σ error level with a further restriction of the optical depth of the 2–1 transition, $\tau \leq 2$. Very high column densities are obtained if the latter condition is not applied. This restriction is in accordance with results of CS isotope observation by Johansson et al. (1994) which show low optical depths of the main isotope towards N 159-W. For $n({\rm H_2}) = 10^{5.5}$ cm^{-3} the kinetic temperatures are less than 25 K for all sources but one, N 66 c2. Lower densities give higher temperatures, however, the CS column densities are basically within the ranges defined by $n({\rm H_2}) \geq 3 \times 10^5$ cm^{-3}.

4. Results

Figure 2 shows graphic representations of the solutions for SMC-B1#1 and Lirs 36 for fixed [^{12}CO/^{13}CO] ratios and molecular hydrogen densities. SMC-B1#1 is a source with a small $\chi^2_{\rm min}$ while Lirs 36 has $\chi^2_{\rm min} > 5$. The corresponding ranges of solutions are defined by $\chi^2 \leq 5$ and $\chi^2 \leq 2\chi^2_{\rm min}$, respectively.

4.1. [^{12}CO/^{13}CO] abundance ratios

Knowledge of the [^{12}CO/^{13}CO] abundance ratio in the Magellanic Clouds would constrain the solutions further. From CS and HCO$^+$ data, Johansson et al. (1994) estimated, for N 159-W in the LMC, a gas phase [^{12}C/^{13}C] abundance ratio in the range 30–75. This is similar to what is observed in the solar neighborhood (Langer & Penzias 1990). Using HCO$^+$ and H^{13}CO$^+$ Heikkilä et al. (1999) estimated the gas-phase ^{12}C/^{13}C ratio to be in the 40–90 range for Lirs 49 in the SMC. For a set of clouds that contains among others, Lirs 49 in the SMC and N 159W, N159S and 30 Dor-10 in the LMC, they derived a [^{12}CO/^{13}CO] abundance ratio of 20–40. Based on metallicity arguments, Lequeux et al. (1994) adopted a [^{12}C/^{13}C] ratio larger than 100 in their modelling of SMC clouds. Extensive modelling by van Dishoeck & Black (1988) shows that the [^{12}C/^{13}C] and [^{12}CO/^{13}CO] ratios are similar in dense clouds but can be significantly different in less dense objects if either of the two processes that work in the opposite direction is

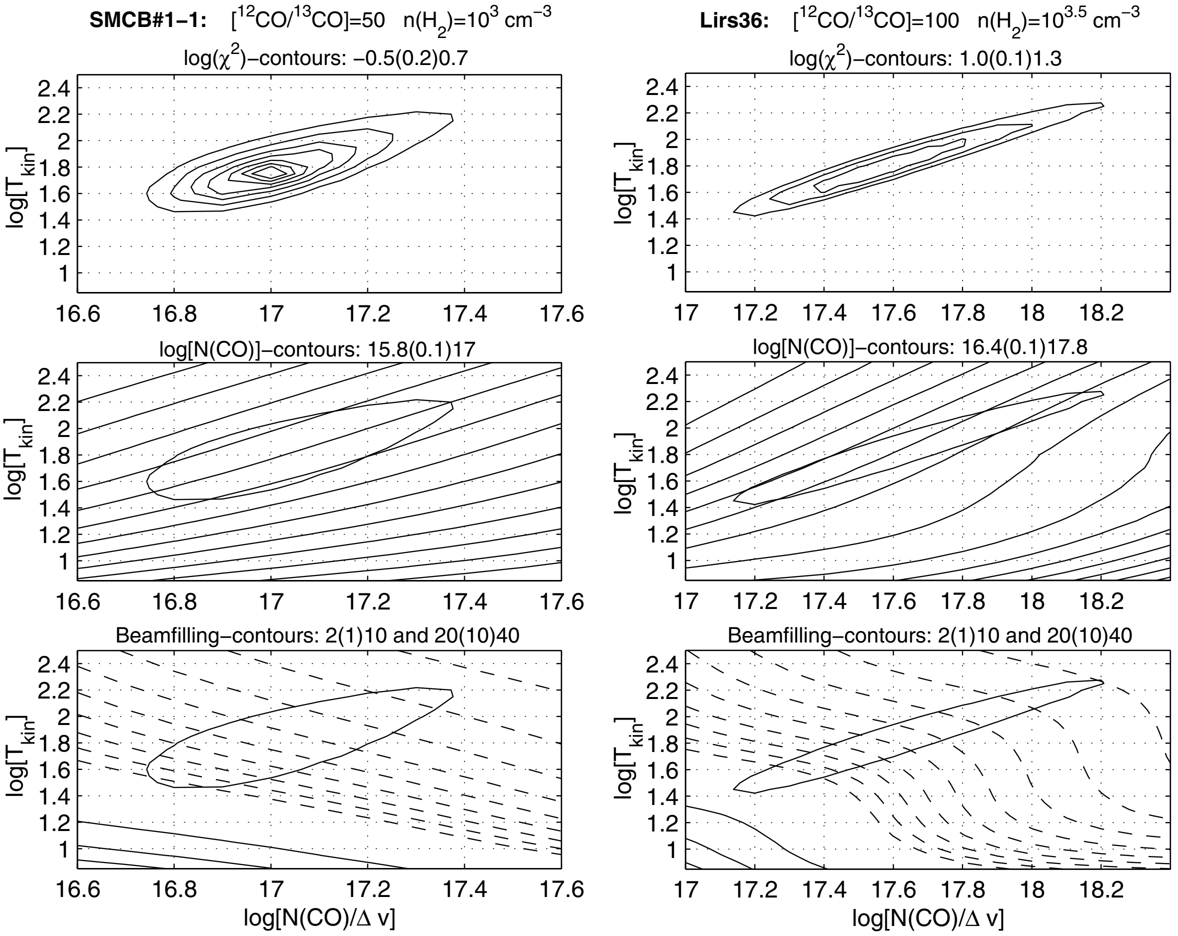

Fig. 2. RADEX solutions for SMC-B1#1 (*left*) and Lirs 36 (*right*). The upper panels show the χ^2 contours on a logarithmic scale in steps of 0.2 (SMC-B1#1) and 0.1 (Lirs 36). The last contour is 0.7 (χ^2 = 5) for SMC-B1#1 and 1.3 (χ^2 = 20; twice the minimum value) for Lirs 36. The middle panels show CO column density contours in steps of 0.1. The leftmost contours correspond to the smaller values. The lower panel gives the contours of the surface filling factor in % where contour levels increase from the upper right corner. The dashed contours are in a step of 1, while the full lines are with a step of 10; the ranges are indicated above the panels. In the two lower panels the χ^2 contours restricting the range of solutions are overlayed. These solutions are for [^{12}CO/^{13}CO] = 50 and n(H$_2$) = 10^3 cm^{-3} (SMC-B1#1), and [^{12}CO/^{13}CO] = 100 and n(H$_2$) = $10^{3.5}$ cm^{-3} (Lirs 36). N(CO) is in units of [cm^{-2}], Δv in [km s^{-1}] and $T_{\rm kin}$ in [K].

dominant – isotope-selective photodissociation or low-temperature carbon isotope exchange reactions. Based on the intense UV-radiation fields in the Magellanic Clouds one would expect the latter reaction, if any, to dominate which would give higher [^{12}CO/^{13}CO] ratios relative to those of [^{12}C/^{13}C]. Anyway all this suggests that, at present, CO isotope data for the Magellanic Clouds are not accurate enough to allow a fixed value in the calculations.

To investigate the impact of the isotopic ratio on the solutions we ran our χ^2 code for [^{12}CO/^{13}CO] ratios between 5 and 300 with a logarithmic step of 0.1. This was done for a range of hydrogen densities n(H$_2$) = 10^3–10^5 cm^{-3}. Each combination of a [^{12}CO/^{13}CO] ratio and number density defines a minimum χ^2 value and the corresponding kinetic temperature and CO column density within the parameter space previously defined. Figures 3 and 4 show the results of such runs for SMC-B1#1 and Lirs 36, respectively. While the χ^2 versus isotope ratio plots show distinctly different characteristics for the two sources, the remaining plots are qualitatively similar. According to the χ^2 variations we distinguish two types of sources:

Class A sources – the SMC-B1#1 type: the general features are absolute χ^2 minima for low densities at an isotope ratio of about 50 or higher, while the χ^2 decrease continuously with isotope ratio at densities n(H$_2$) $\gtrsim 10^4$. The only other member of this class in the present sample is N 159-S in the LMC. However, in the LMC there are other examples of clouds of this type (Johansson et al., in prep.).

Class B sources – the Lirs 36 type: local or, in some cases, absolute minima at all densities and small isotope ratios, generally less than 20. With the exception of Lirs 49 c2 (see Fig. 5), which seems to be an intermediate case, all the remaining sources in our sample can be assigned to this class.

Common for both classes of sources is that the derived CO column densities are largely independent of the hydrogen densities but scale with the isotope ratio applied. For n(H$_2$) $\gtrsim 10^4$ cm^{-3}, the kinetic temperatures are relatively well confined as are the surface filling factor of the CO emission over a large range of isotope ratios, properties applying to the sample as a whole.

Using the isotope ratio plots, we have assigned formal solutions of the [^{12}CO/^{13}CO] ratio and n(H$_2$) for each source. The results are presented in Table 3. We rejected solutions with [^{12}CO/^{13}CO] ≤ 30, and when no minima are present we set an upper limit of the ratio to 100; higher ratios do not change the kinetic temperature nor the surface filling factor significantly,

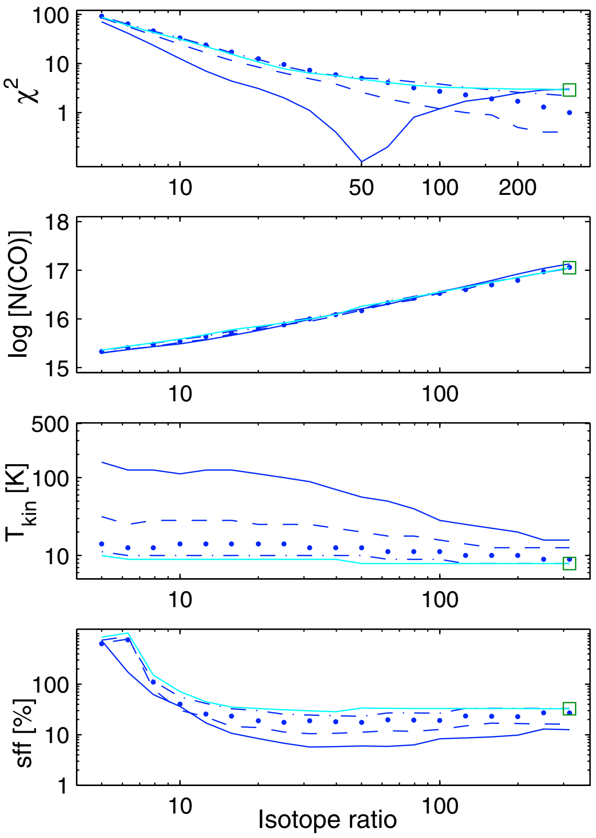

Fig. 3. SMC-B1#1: minimum χ^2 solutions as a function of the [^{12}CO/^{13}CO] ratio at different hydrogen densities $n(H_2)$ = 10^3 cm^{-3} (black solid), $10^{3.5}$ cm^{-3} (dash), 10^4 cm^{-3} (dot), $10^{4.5}$ cm^{-3} (dash-dot) and 10^5 cm^{-3} (grey solid with a square at the highest ratio). N(CO) is in units of cm^{-2}.

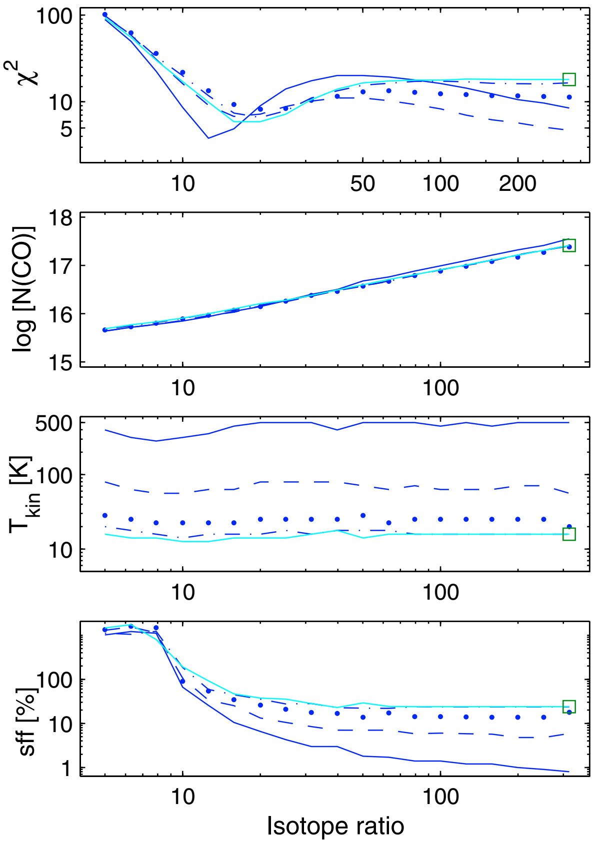

Fig. 4. Lirs 36: minimum χ^2 solutions as a function of the [^{12}CO/^{13}CO] ratio at different hydrogen densities. The $n(H_2)$ densities legend and the N(CO) units as in Fig. 3.

while the CO column density scales linearly with the isotopic ratio.

For each source we give the two best solutions with different hydrogen densities (three in some cases) obtained from the χ^2 analysis. This provides a hint on the CO excitation conditions in different environments. There is a tendency for higher hydrogen densities and lower filling factors in sources close to regions of vigorous star formation, e.g., N 66 and 30 Dor–10, than in the rest of the sample. One explanation could be a higher CO dissociation rate in the former sources, forcing the surviving CO to be in higher density regions. We note, however, that the χ^2 values are high in most of these cases, casting some doubt on such an interpretation. More reliable are the CO column density results which are less sensitive to the hydrogen density and, accordingly, to the kinetic temperature.

Provided that the [^{12}CO/^{13}CO] ratios are similar in the Magellanic Clouds, LMC clouds have CO column densities an order of magnitude larger than SMC clouds. A similar factor applies to the CS data. For clouds of similar linear sizes but smaller than the beam, the larger distance to the SMC could account for a factor of 1.4, at most. In case of CO, the column density difference between the LMC and the SMC scales directly with a possible difference of the [^{12}CO/^{13}CO] ratios in the two objects.

5. Discussion

Due to the limited information available from relative intensities rather than a data set of absolute intensities, low and high optical depth solutions might be quite indistinguishable. The local χ^2 minima at low isotope ratios for the Class B sources (see Fig. 4) are most likely a manifestation of such an effect. Within the investigated isotope range four sources, N 66 c2, N88, Lirs 49 c1 in the SMC and 30 Dor–10 (LMC), even have absolute minima at low ratios. All these minima fall close to the observed antenna temperature ratios of isotopic species, ^{12}CO/^{13}CO ≈ 10, implying low optical depth solutions. So far, such small CO isotope ratios have only been observed in some planetary nebula (e.g., Rubin et al. 2004) and circumstellar shells of late type stars (e.g., Josselin & Lébre 2001) and for molecular clouds we consider them to be unrealistically low. The rejection of low isotope ratio solutions is further emphasized by the simulations below.

5.1. Simulations: 1-component model

As pointed out earlier on, the Class A sources SMC-B1#1 and N 159-S have χ^2 minima at [^{12}CO/^{13}CO] ≈ 50. The isotope ratio plots of N 159-S are very similar to those of SMC-B1#1 (Fig. 3) but have more pronounced χ^2 minima. Both clouds are considered to be at quiescent locations, since they are far away from H II regions and lack significant internal heating sources. The formal solutions for the isotope ratios and molecular hydrogen densities (Table 3) give, however, kinetic temperatures similar to, or higher, than for sources presumably associated with hotter environments. IRAS data for N 159-S point to an upper limit of dust temperature of 25 K (Bolatto et al. 2000a). SMC-B1#1 is below the IRAS detection limit (Lequeux et al. 1994). For the

Table 3. RADEX solutions. The observed intensities for the LMC are taken from Johansson et al. (1994, 1998) and Heikkilä et al. (1999). Numbers in brackets are ranges as defined by $\chi^2 \leq 2\,\chi^2_{\rm min}$, see Sect. 3.3 for more details.

	n(H$_2$) [cm^{-3}]	CO/^{13}CO	$T_{\rm kin}$ [K]	$N_{\rm CO}$ [10^{16} cm^{-2}]	filling [%]	χ^2	$N_{\rm CS}$ [10^{12} cm^{-2}]
N 66 c1	$10^{4.5}$	100	160 (≥20)	0.8 (≥0.1)	1.0 (≤15)	9.7	≤0.4
	10^4	100	220 (≥30)	0.5 (≥0.1)	1.0 (≤15)	12	
N 66 c2	10^4	100	90 (≥25)	5.4 (≥3.3)	1.0 (≤4.0)	6.3	0.6–2.5
	$10^{4.5}$	100	75 (≥0)	7.2 (≥3.5)	1.0 (≤6.0)	7.0	
N 88	$10^{3.5}$	100	≥15	≥2.0	≤7.0	28	0.6–3.2
	10^4	100	60 (≥10)	4.5 (≥1.9)	1.0 (≤12)	34	
Lirs 36	$10^{3.5}$	100	63 (25–240)	7.9 (6.3–12)	6.0 (1.5–15)	10	1.0–4.0
	10^4	100	25 (13–63)	7.4 (5.9–9.3)	14 (5.0–32)	15	
Lirs 49 c1	10^4	100	40 (17–125)	9.1 (6.9–13)	6.0 (1.5–15)	12	1.2–8.0
	$10^{3.5}$	100	110 (≥35)	9.3 (≥6.9)	2.5 (≤8)	13	
Lirs 49 c2[a]	$10^{3.5}$	100	33 (15–300)	1.8 (1.3–4.0)	1.0 (≤3.0)	0.9	0.4–10
	10^4	100	14 (11–23)	1.8 (1.5–2.2)	2.5 (1.5–4.0)	2.9	
Hodge 15	$10^{3.5}$	100	30 (18–65)	4.7 (3.8–5.8)	4.0 (2.0–8.0)	4.6	≤1.8[b]
	10^3	100	125 (≥35)	5.8 (≥4.1)	1.5 (≤6.0)	5.6	
SMC-B1#1[a]	10^3	50	56 (30–170)	1.6 (1.2–2.1)	6.0 (2.5–11)	0.13	0.4–8.0
	$10^{3.5}$	100	16 (12–20)	3.3 (2.5–4.2)	13 (8.5–20)	1.3	
	10^3	100	30 (20–55)	3.5 (2.6–4.7)	7.5 (4–13)	1.4	
LMC							
30 Dor-10	$10^{4.5}$	100	125 (≥15)	23 (≥8.3)	1.5 (≤20)	18	4–16
	10^4	100	145 (≥16)	17 (≥7.6)	1.5 (≤15)	19	
N 159-W	$10^{3.5}$	100	200 (≥45)	110 (≥70)	5 (≤20)	4.0	10–32
	10^4	100	28 (15–95)	80 (60–120)	30 (9.0–70)	8.2	
N 159-S[a]	10^3	50	125 (≥43)	20 (≥16)	14 (≤30)	1.3	10–130
	$10^{3.5}$	100	19 (14–25)	41 (35–47)	43 (32–60)	3.6	
	10^4	100	11 (10–14)	42 (36–47)	85 (62–100)	3.7	

[a] The CO ranges are defined by $\chi^2 = 5$. [b] LTE column density from the observed CS(3–2) transition assuming $T_{\rm ex} \geq 5$ K and $\tau \leq 2$.

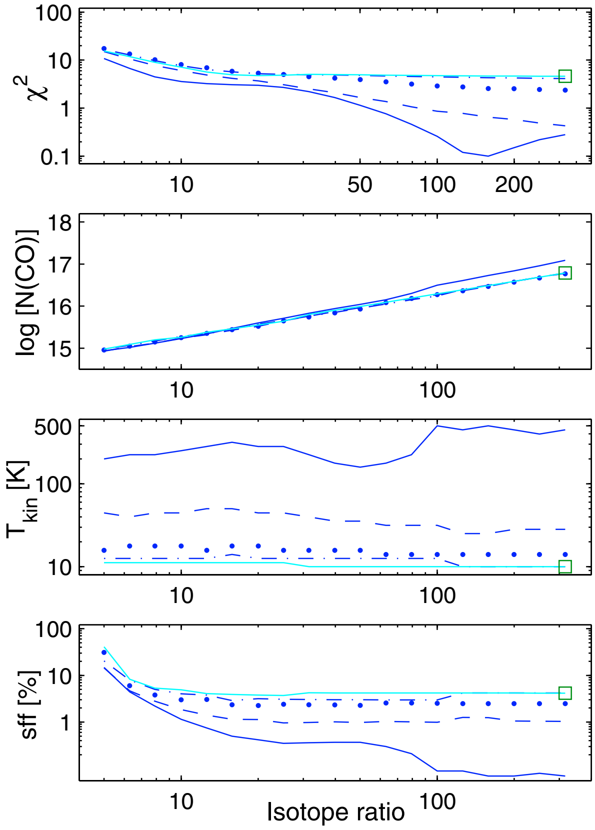

Fig. 5. Lirs 49 c2: minimum χ^2 solutions as a function of the [^{12}CO/^{13}CO] ratio at different hydrogen densities. The n(H$_2$) densities legend and the N(CO) units as in Fig. 3.

dust in the diffuse medium of the SMC a reference equilibrium temperature is found to be (22 ± 2) K (Bot et al. 2004). However, the high temperature solutions are associated with low volume densities which means less coupling between gas and dust.

Using the SMC-B1#1 data we investigated whether other combinations of n(H$_2$) and [^{12}CO/^{13}CO] ratios can produce similar isotope ratio plots by performing the following simulations. Using a random noise generator giving similar uncertainties as those of the observations, we added noise to the RADEX output of models with a number of possible formal solutions for SMC-B1#1 according to Fig. 3. Each model was simulated 50 times with different noise contributions and the results averaged. The average χ^2 plots for three models of different combinations of n(H$_2$) and [^{12}CO/^{13}CO] ratios are shown in Fig. 6. The most prominent feature in plots with model [^{12}CO/^{13}CO] ratios larger than 50 are ratios close to 50 for n(H$_2$) = 10^3 cm^{-3} independent of model parameters. Less prominent χ^2 minima coincide with the model values. Reducing the errors of the input data give local minima at different densities, however, the absolute χ^2 minima give the correct results. All the simulations show that the minima for n(H$_2$) = 10^3 cm^{-3} are lower limits of the actual isotope ratio, i.e., our data suggest that [^{12}CO/^{13}CO] ≥ 50 in the Magellanic Clouds. Isotope ratios and molecular hydrogen densities larger than 50 and 10^3 cm^{-3}, respectively, explain well the observed CO data for the class A sources. Such parameter values would result in kinetic temperatures lower than those of the, formally, best solutions given in Table 3. However, at present, we can not exclude the high-temperature solutions of these sources. On the other hand, the CO column density is largely independent of the molecular hydrogen density and, accordingly, the kinetic temperature as well, and scales with the isotope ratio.

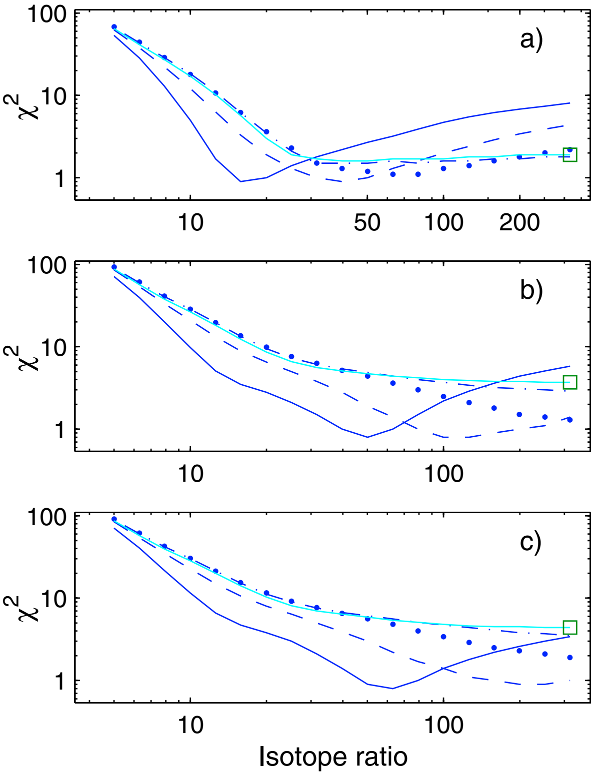

Fig. 6. Average χ^2 plots from SMC-B1#1 simulations of different combinations of ^{12}CO/^{13}CO ratios and $n(H_2)$ densities. Each plot is the result of 50 simulations of different noise contributions generated randomly with statistics in accordance with the estimated observational errors. Input data are: **a)** model: [^{12}CO/^{13}CO] = 40, $n(H_2) = 10^{3.5}$ cm^{-3}, $T_{\rm kin}$ = 20 K and N(CO) = 4×10^{16} cm^{-2}; **b)** model: [^{12}CO/^{13}CO] = 100, $n(H_2) = 10^{3.5}$ cm^{-3}, $T_{\rm kin}$ = 15.9 K and N(CO) = 10^{17} cm^{-2}; **c)** model: [^{12}CO/^{13}CO] = 200, $n(H_2) = 10^{3.5}$ cm^{-3}, $T_{\rm kin}$ = 12.6 K and N(CO) = 1.6×10^{17} cm^{-2}. The $n(H_2)$ densities legend is given in the Fig. 3 caption.

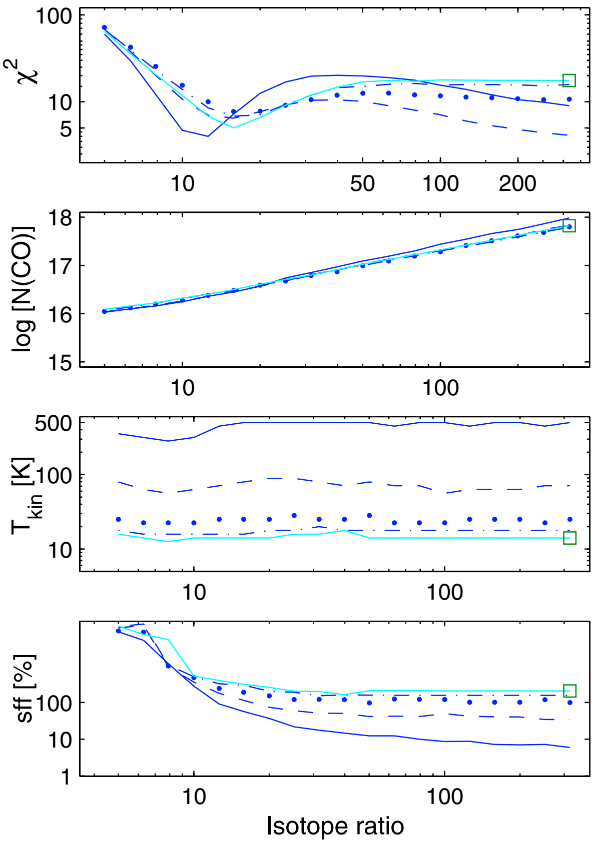

Fig. 7. 2-component model of Lirs 36: minimum χ^2 solutions as a function of the ^{12}CO/^{13}CO ratio at different $n(H_2)$ densities. The model parameters are: the isotope ratio [^{12}CO/^{13}CO] = 100, $T_{\rm kin1}$ = 20 K, $T_{\rm kin2}$ = 100 K, $n(H_2)_1 = 10^4$ cm^{-3}, $n(H_2)_2 = 10^{3.5}$ cm^{-3}, and $N(CO)_1 = 2 \times 10^{17}$ cm^{-2} and $N(CO)_2 = 5 \times 10^{15}$ cm^{-2}. The $n(H_2)$ densities legend is given in the Fig. 3 caption.

5.2. Simulations: 2-component model

The existence of a warm, low density and widespread CO component in the Magellanic Clouds has been suggested by Israel et al. (2003), and more recently inferred from AST/RO CO(4–3) observations and 2-component modelling of the gas by Bolatto et al. (2005). The high χ^2 values for the majority of sources in our sample (see Table 3) strongly suggest that a model of constant physical parameters immersed in the cosmic microwave background can not represent the actual cloud conditions. Below we show, taking Lirs 36 as representative, that the observed intensities and the main Class B feature, pronounced χ^2 minima at low isotope ratios, can be reproduced by a 2-component gas model with larger isotope ratios.

We assume that the two CO gas components are radiatively decoupled, i.e., the 2-component model consists of the sum of the radiation temperatures from two separate RADEX runs with different input parameters. This assumption is a reasonable approximation for an environment of low surface filling factors of both components (i.e., small shielding) or for one component with large filling factor and low optical depth. The limited observational data set for each cloud does not allow us to obtain a unique solution; many different parameter combinations will give results that resemble the observed ones. The particular model assumes the presence of a cold, dense component and a warmer, lower density component. We simplify the choice of parameters by fixing the isotope ratio to 100, the kinetic temperatures of each component to 20 K and 100 K, and the molecular hydrogen density of the cold component to 10^4 cm^{-3}. In addition, we use complete beam filling for both components. The two CO column densities and the hydrogen density of the warm component are then derived from a comparison with the observed CO intensity ratios.

With the above set of fixed values we find that the molecular emission from Lirs 36 can be explained as arising from a mixture of a dominating cold component with N(CO) = 2×10^{17} cm^{-2} and a warm component with $n(H_2) \approx 3 \times 10^3$ cm^{-3} and N(CO) = 5×10^{15} cm^{-2}. Figure 7 shows the isotope dependent plots for this set of parameters, resembling well all the characteristics of the Class B sources (see Fig. 4). We stress, however, that this is not a unique solution.

Our simulations using a 2-component gas models show that the local χ^2 minima at low isotope ratios is a result of a medium with temperature and/or density gradients. Such minima are low optical depth solutions forced by the observed ^{12}CO/^{13}CO intensity ratios. The 2-component modelling also indicates that the kinetic temperature and surface filling factor of the dominant component are well determined provided that the $n(H_2)$ density and the isotope ratio are known within a factor of about two (see Fig. 7). On the other hand, the χ^2 plot itself does not provide any reliable information on these latter parameters.

Finally, it is interesting to note that Hodge 15, considered to be a quiescent cold cloud, shows the Class B features

Table 4. Parameter constraints from 2-component modelling using [^{12}CO/^{13}CO] = 100. The notation "all" means that there are no constraints within the investigated ranges.

	Cold phase		Warm phase			
Cloud	n(H$_2$) [cm^{-3}]	$T_{\rm kin}$ [K]	n(H$_2$) [cm^{-3}]	$T_{\rm kin}$ [K]	χ^2	Classification
N 66 c1	all	all	$\gtrsim 10^4$	$\gtrsim 200$	4.8	Warm dense
N 66 c2	$\gtrsim 10^4$	30–100	$\gtrsim 3 \times 10^3$	$\gtrsim 50$	0.04	Warm diffuse
N88	$\gtrsim 3 \times 10^3$	20–100	$\gtrsim 10^4$	$\gtrsim 200$	0.09	Warm dense
Lirs 36	$\gtrsim 3 \times 10^3$	10–100	$> 10^3$	$\gtrsim 20$	0.03	Mixed
Lirs 49 c1	$\gtrsim 3 \times 10^3$	10–100	$> 10^3$	$\gtrsim 20$	0.06	Mixed
Lirs 49 c2	all	all	all	all	0.01	Mixed
Hodge 15	$\gtrsim 3 \times 10^3$	$\lesssim 20$	$\lesssim 3 \times 10^4$	all	0.14	Mixed
SMC-B1#1	$\lesssim 3 \times 10^4$	~ 10	$\lesssim 3 \times 10^3$	20–100	0.03	Warm diffuse
30 Dor-10	$\gtrsim 3 \times 10^3$	30–100	$\gtrsim 10^4$	$\gtrsim 100$	2.7	Warm dense
N 159-W	$> 10^3$	10–100	$\gtrsim 3 \times 10^3$	$\gtrsim 100$	1.2	Warm dense
N 159-S	all	$\lesssim 20$	$\lesssim 3 \times 10^3$	$\gtrsim 20$	0.5	Warm diffuse

indicating a medium of gas parameters characterised by significant gradients.

5.3. Source classification from a 2-component code

Using the 2-component code we made an attempt to constrain the model parameters for each source by searching for combinations of parameters that give the smallest χ^2 value. The parameter space investigated is limited by adopting a fixed [^{12}CO/^{13}CO] ratio and assuming equal surface filling factor of the two gas phases. Neither condition is necessarily true, e.g., isotope selective photodissociation could well separate the two components with respect to the [^{12}CO/^{13}CO] ratio. Also, there is no reason to believe that the filling factors are equal, but variations of the remaining parameters can partly compensate for this (see below); in the end the relative weight of the components is determined by the CO intensities. Additionally, in accordance with the previous discussion we assume that the two components are radiatively decoupled.

For the molecular hydrogen densities we use the same logarithmic range and step as used in Sect. 3.2. Slightly smaller ranges were used for the kinetic temperatures and ^{12}CO column densities, 10–300 K and 3×10^{14} to 10^{19} cm^{-2}, respectively, with a logarithmic step of 0.1 for both. For each combination of two hydrogen densities, our code picks out the solution with the smallest χ^2 value in the kinetic temperature and the CO column density ranges given above. The range of the solutions is that in which $\chi^2 \lesssim 1$ and when $\chi^2_{\rm min} \gtrsim 1$ we use $\chi^2 \lesssim 2\,\chi^2_{\rm min}$.

Table 4 gives the results for [^{12}CO/^{13}CO] = 100. Columns 2 and 4 give the constraints in n(H$_2$), and Cols. 3 and 5 those in $T_{\rm kin}$, for the cold and warm components, respectively. The notation "all" indicates that the range investigated can not be restricted. The tabulated constraints are defined by *the best solutions for each combination of two hydrogen densities*, i.e., secondary minima that satisfy the χ^2 constraints are lost. In four sources, for all combinations of hydrogen densities allowed by the χ^2 restrictions, the warmer component is the denser. We label such sources "warm dense" (Col. 7). For three sources, labeled as "warm diffuse", the opposite is true, i.e., the colder component is the denser one. The remaining sources show both properties, i.e., some density combinations have the "warm dense" characteristics and others the "warm diffuse". Those are labeled "mixed", a notation simply indicating that our model is unable to classify the source whether the reason is, e.g., large observational errors and/or unfavourable source structures with respect to the model.

To assess the role of our assumptions in the inferred cloud type we have run a few simulations including gas phases with different surface filling factors. In particular, in one simulation, referred as hot core type, we adopted for the two components surface filling factors of 100 and 20%, H$_2$ densities of 10^3 and 10^4 cm^{-3} and kinetic temperatures of and 20 and 100 K, respectively. Both components have the same [^{12}CO/^{13}CO] ratio (100) and column density (10^{17} cm^{-2}). The total column density, corrected for surface filling factors, is then 1.2×10^{17} cm^{-2}. The applied observational errors are consistent with those of our observations. Our code (correctly) classifies this object as "warm dense" with a total column density of 1.5×10^{17} cm^{-2} and a filling factor of 50%. The best solution is for n(H$_2$) = 10^3 and $10^{3.5}$, $T_{\rm kin}$ = 13 and 126 K, and N(CO) = 2.5×10^{17} and 0.5×10^{17}. In the case of two distinct gas phases, we expect the classification to come out correctly, independent of surface filling factors, provided that the observed CO emissions from both components are significantly larger than the observational errors.

If we adopt [^{12}CO/^{13}CO] = 50, the classification of all sources remains the same with a slightly different range of constraints. The resulting CO column densities agree with those presented for the 1-component modelling and scale with the isotope ratio applied. This is also the case for the filling factors.

The two Class A sources, SMC-B1#1 and N 159-S, belong to the "warm diffuse" group. Most sources generally expected to be associated with regions of vigorous star formation fall in the "warm dense" category. Among the latter, there is an overall agreement with the results of 2-component fits of Bolatto et al. (2005). The only exception is N 159-W. For this source their model, with a fixed [^{12}CO/^{13}CO] = 40, gives a cold dense component with n(H$_2$) = 10^5 cm^{-3} and $T_{\rm kin}$ = 20 K, and a very tenuous phase with n(H$_2$) = 10^2 cm^{-3} and $T_{\rm kin}$ = 100 K. If we fit their model to our CO data we get a poor $\chi^2 = 22$ (to be compared with $\chi^2 = 1$ for the "warm dense" model). Their input data set consists of a compilation of the published data of Johansson et al. (1998), Bolatto et al. (2000b), Chin et al. (1998), Heikkilä et al. (1999), and Rubio et al. (1993, 1996), and the newly observed ^{12}CO (4–3) transition. What might be crucial and could explain the discrepancy of the results is the spatial resolution. While we refer to a beam size of 45″, the Bolatto et al. (2005) data are convolved to the CO (4–3) resolution of 109″. Thus, a model consisting of a hot core of limited extent with widespread components of cold gas as well as a hot and tenuous component is probably in line with both interpretations since the CO intensities of the hot core would be about 6 times lower in the larger beam.

5.4. Column densities

Column densities derived from both the 1-component and 2-component models are determined with good accuracy and scale linearly with the [^{12}CO/^{13}CO] ratio. The CO column densities presented in Table 3 are typically a factor of 5 higher than those previously published (e.g., Chin et al. 1998; Johansson et al. 1998; and Heikkilä et al. 1999). This discrepancy is explained in terms of the higher [^{12}CO/^{13}CO] ratios used in this work. In contrast, the CS data agree well with previous determinations (e.g., Chin et al. 1998; Heikkilä et al. 1999).

As pointed out in Sect. 4, if similar types of clouds are considered, like SMC-B1#1 (SMC) and N 159-S (LMC), CO column densities are larger by a factor of about 10 in the LMC relative to the SMC. A similar factor applies to the strongest CO emitters associated with HII regions, Lirs 49 c1 and Lirs 36 in the SMC, and N 159-W in the LMC. 30 Dor-10 (LMC) is located in the most extreme environment while N 66 c1, c2 and N 88 have less accurate column densities. Note that this factor of ≈10 assumes similar [^{12}CO/^{13}CO] ratios in the two Clouds.

The CS column densities are more stable with respect to environments and show a similar difference as CO suggesting a connection with the metallicity difference between the SMC and the LMC.

5.5. Surface filling factors and kinetic temperatures

The derived filling factors and kinetic temperatures of CO are strongly dependent on the molecular hydrogen density as long as the latter is close to the critical density for excitation of the higher CO transitions. In an attempt to identify trends we use here the best solutions (with respect to χ^2 numbers) in Table 3 with the assumption that the ^{12}CO/^{13}CO is constant throughout our sample. Then the surface filling factor of the CO emission seems to be larger in the LMC than in the SMC. In the LMC there is a strong trend of lower filling factors with increasing star formation activity. A similar trend, however less obvious, might exist in the SMC indicated by the most extreme environments as suggested by star formation activities, i.e., N 66 and N 88 on one hand and SMC-B1#1 on the other. This is in accordance with the results of Lequeux et al. (1994). Using the same SMC sample they obtained a surface filling factor of less than 10% for the "hottest" clouds.

6. Summary and conclusions

We present and analyse ^{12}CO, ^{13}CO, and CS multi-transitional observations of six SMC clouds, N 88, N 66, Lirs 36, Lirs 49, Hodge 15, and SMC-B1#1. In order to compare clouds of similar properties in the two galaxies the same method was used to re-analyse data of three clouds in the LMC, 30 Dor-10, N159-W, and N159-S (Johansson et al. 1998). Clouds were modelled as being spherical, homogeneous and isothermal with constant densities and abundances, immersed in the cosmic microwave background radiation field. The model uses the mean escape probability approximation for the radiative transfer equations.

The derived CO column densities are largely independent of the molecular hydrogen densities used in the calculations and scale with the [^{12}CO/^{13}CO] ratio adopted. They are typically a factor of five higher than those previously published for some of the clouds, a discrepancy explained in terms of the higher [^{12}CO/^{13}CO] ratio used in this paper.

Contrary to the column densities, the derived surface filling factors, *sff*, and kinetic temperatures of CO are strongly dependent on the molecular hydrogen density. We find that in the SMC the *sff* is generally low, with upper limits of ~10−20%, and seems to be a factor of a few larger in the LMC. With increasing star formation activity, i.e., increasing UV radiation fields as indicated by optical and radio tracers of star formation activity, the surface filling factors tend to decrease. This is most obvious in the LMC but a similar trend exists in the SMC, as suggested by the two extremes with respect to star-formation activities, i.e., N 66 and N 88 on one hand and SMC-B1#1 on the other.

If similar types of clouds are considered, CO column densities seem to be larger by a factor of about 10 in the LMC relative those of the SMC. CS is more stable with varying environments, but nevertheless shows similar differences. Since the larger distance to the SMC could account only for a factor of 1.4 at most, the discrepancy rather mirrors the metallicity difference between the two galaxies.

Defined by the χ^2 variations, we have identified two classes of sources, denoted as Class A and B. Class A objects – SMC-B1#1 in the SMC and N 159-S in the LMC, are well described by a simple model consisting of a uniform, single gas component. The simulations indicate a lower limit of the ^{12}CO/^{13}CO isotopic ratio of about 50. Minimum χ^2 values for SMC-B1#1 and N 159-S are produced by models with this isotopic ratio, $n(\mathrm{H_2}) = 10^3$ cm^{-3} and $T_{\mathrm{kin}} \geq 50$ K. However, simulations show that the observed CO intensities can also be well described by models with higher ^{12}CO/^{13}CO ratios and densities and lower kinetic temperatures.

Class B objects include Lirs 36 (the prototype), N 66 (both velocity components), N 88, Lirs 49 c1, Hodge 15 in the SMC and 30 Dor-10, and N159-W in the LMC. The χ^2 versus isotope ratio plots for these objects show pronounced minima at [^{12}CO/^{13}CO] ratios less than ~30; however, the high values of χ^2 strongly indicate that the simple model is a poor approximation to the actual conditions of the environments. Using a 2-component model we can reproduce the χ^2 behaviour with significantly higher ^{12}CO/^{13}CO ratios suggesting that these minima are a signature of the presence of gas gradients and low optical depth solutions forced by the observed ^{12}CO/^{13}CO brightness temperature ratios. A model consisting of a cold and dense component with $T_{\mathrm{kin}} = 20$ K, $n(\mathrm{H_2}) = 10^4$ cm^{-3} and $N(\mathrm{CO}) = 2 \times 10^{17}$ cm^{-2} and a warmer and less dense component with $T_{\mathrm{kin}} = 100$ K, $n(\mathrm{H_2}) = 3 \times 10^3$ cm^{-3} and $N(\mathrm{CO}) = 5 \times 10^{15}$ cm^{-2}, accurately reproduces all the observed characteristics of the Lirs 36 CO emission. This is not, however, a unique solution.

Assuming a fixed [^{12}CO/^{13}CO] ratio, two radiatively decoupled gas phase components of equal surface filling factors, we have made an attempt to constrain the model parameters for each source. Tentative results show that the majority of the clouds considered can either be classified as "hot core" type objects, where the warmer gas component is the denser one, or "hot envelopes" objects, where the warmer gas phase is more diffuse. The first group of clouds consists of N 66 c1, N 88, 30 Dor-10, and N 159-W, the latter defines N 66 c2, SMC-B1#1, and N 159-S, while Lirs 36, Lirs 49 and Hodge 15 can not be assigned to any group.

We performed a few simulations in which the two components have different surface filling factors. These simulations indicate that the classification type is robust provided that the CO emission from both components is large relative to the applied observational error, and that the two components have distinctively different physical properties. A larger number of simulations is required to quantify the accuracy of our classification.

Acknowledgements. S.N., G.G. and M.R. acknowledge support form the Chilean *Centro de Astrofísica* FONDAP No. 15010003. M.R. acknowledges the Fondecyt (Chile) grant No. 1960926.

References

Bolatto, A. D., Jackson, J. M., Israel, F. P., et al. 2000a, ApJ, 545, 234

Bolatto, A. D., Jackson, J. M., Kraemer, K. E., & Zhang, X. 2000b, ApJ, 541, L17

Bolatto, A. D., Israel, F. P., & Martin, C. L. 2005, ApJ, 633, 210

Bot, C., Boulanger, F., Lagache, G., Cambrésy, L., & Egret, D. 2004, A&A, 423, 567

Caplan, J., Ye, T., Deharveng, L., Turtle, A. J., & Kennicutt, R. C. 1996, A&A, 307, 403

Clayton, G. C., Wolff, M. J., Sofia, U. J., Gordon, K. D., & Misselt, K. A. 2003, ApJ, 588, 871

Chin, Y.-N., Henkel, C., Millar, T. J., et al. 1998, A&A, 330, 90

Davies, R. D., Elliot, K. H., & Meaburm, J. 1976, MNRAS, 81, 89

Flower, D. R. 2001, J. Phys. B., 34, 2731

Gordon, K. D., Clayton, G. C., Misselt, K. A., Landolt, A. U., & Wolff, M. J. 2003, ApJ, 594, 279

Green, S., & Chapman, S. 1978, ApJS, 37, 169

Heikkilä, A., Johansson, L. E. B., & Olofsson, H. 1999, A&A, 344, 817

Henize, K. G. 1956, ApJS, 2, 315

Hodge, P. W. 1974, PASP, 86, 263

Israel, F. P., Johansson, L. E. B., Lequeux, J., et al. 1993, A&A, 276, 25

Israel, F. P., Johansson, L. E. B., Rubio, M., et al. 2003, A&A, 406, 817

Jansen, D., van Dishoeck, E. F., & Black, J. H. 1994, A&A, 282, 605

Johansson, L. E. B., Olofsson, H., Hjalmarson, Å., et al. 1994, A&A, 291, 89

Johansson, L. E. B., Greve, A., Booth, R. S., et al. 1998, A&A, 331, 857

Josselin, E., & Lébre, A. 2001, A&A, 367, 826

Lequeux, J., Le Bourlot, J., Pineau des Forets, G., et al. 1994, A&A, 292, 371

Piatti, A. E., Sautzeff, N. B., Geisler, D., Seguel, J., & Clark, D. 2005, MNRAS, 358, 1215

Rubin, R. H., Ferland, G. J., Chollet, E. E., & Horstmeyer, R. 2001, ApJ, 605, 784

Rubio, M., Lequeux, J., & Boulanger, F. 1993, A&A, 271, 9

Rubio, M., Lequeux, J., Boulanger, F., et al. 1996, A&ASS, 118, 263

Rubio, M., Contursi, A., Lequeux, J., et al. 2000, A&A, 359, 1139

Rubio, M., Boulanger, F., Rantakyrö, F., & Contursi, A. 2004, A&A, 425, L1

Schinke, R., Engel, V., Buck, U., Meyer, H., & Diercksen, G. H. F. 1985, ApJ, 299, 939

Schöier, F. L., van der Tak, F. F. S., van Dishoeck, E. F., & Black, J. H. 2005, A&A, 432, 369

Schwering, P. B. W., & Israel, F. P. 1989, A&ASS, 79, 79

Turner, B. E., Chan, K., Green, S., & Lubowich, D. A. 1992, ApJ, 399, 114

Westerlund, B. E. 1990, Astron. Astrophys. Rev., 2, 29

Van Dishoeck, E. F., & Black, J. H. 1988, ApJ, 334, 771

Wilke, K., Stickel, M., Haas, U., et al. 2003, A&A, 401, 873

Wilcots, E. M. 1994, AJ, 107, 1338